Connecting Solar Wind Velocity Spikes Measured by Solar Orbiter and Coronal Brightenings Observed by SDO

Chuanpeng Hou, Alexis Rouillard, Jiansen He, Bahaeddine Gannouni, Victor Réville, Philippe Louarn, Andrey Fedorov, Lubomír Přech, Christopher Owen, Daniel Verscharen, et al.

The Astrophysical Journal Letters, 968:L28 (9pp), 2024 June 20 https://doi.org/10.3847/2041-8213/ad4eda

Connecting Solar Wind Velocity Spikes Measured by Solar Orbiter and Coronal Brightenings Observed by SDO

Chuanpeng Hou[1,2], Alexis P. Rouillard[2], Jiansen He[1], Bahaeddine Gannouni[2], Victor Réville[2], Philippe Louarn[2], Andrey Fedorov[2], Lubomír Přech[3], Christopher J. Owen[4], Daniel Verscharen[4], Raffaella D'Amicis[5], Luca Sorriso-Valvo[6,7], Naïs Fargette[8], Jesse Coburn[4,9], Vincent Génot[2], Jim M. Raines[10], Roberto Bruno[5], Stefano Livi[11], Benoit Lavraud[2,12], Nicolas André[2,13], Gabriel Fruit[2], Rungployphan Kieokaew[2], Illya Plotnikov[2], Emmanuel Penou[2], Alain Barthe[15], Dhiren Kataria[11], Matthieu Berthomier[16], Frederic Allegrini[11,14], Vito Fortunato[17], Gennaro Mele[18], and Timothy Horbury[8]

[1] School of Earth and Space Sciences, Peking University, Beijing, 100871, People's Republic of China; jshept@pku.edu.cn
[2] IRAP, Université Toulouse III—Paul Sabatier, CNRS, CNES, Toulouse, France; arouillard@irap.omp.eu
[3] Charles University, Faculty of Mathematics and Physics, V Holešovičkách 2, 180 00 Prague 8, Czech Republic
[4] Mullard Space Science Laboratory, University College London, Holmbury St. Mary, Dorking, Surrey RH5 6NT, UK
[5] INAF-Istituto di Astrofisica e Planetologia Spaziali, Via Fosso del Cavaliere 100, 00133 Roma, Italy
[6] National Research Council, Institute for the Science and Technology of Plasmas, Via Amendola 122/D, 70126 Bari, Italy
[7] Space and Plasma Physics Division, School of Electrical Engineering and Computer Science, KTH Royal Institute of Technology, Teknikringen 31, SE-11428 Stockholm, Sweden
[8] The Blackett Laboratory, Department of Physics, Imperial College London, London SW7 2AZ, UK
[9] Space Science Institute, 4765 Walnut Street, Suite B, Boulder, CO 80301, USA
[10] Department of Climate and Space Sciences and Engineering, The University of Michigan, Ann Arbor, MI, USA
[11] Southwest Research Institute, 6220 Culebra Road, San Antonio, TX 78238, USA
[12] Laboratoire d'astrophysique de Bordeaux, Univ. Bordeaux, CNRS, Pessac, France
[13] Institut Supérieur de l'Aéronautique et de l'Espace (ISAE-SUPAERO), Université de Toulouse, Toulouse, France
[14] Department of Physics and Astronomy, University of Texas at San Antonio, San Antonio, Texas, USA
[15] AKKA, Toulouse, France
[16] Laboratoire de Physique des Plasmas, Ecole Polytechnique, Palaiseau, France
[17] Planetek Italia S.r.l., Via Massaua, 12, 70132 Bari BA, Italy
[18] Leonardo, Viale del lavoro, 101, 74123 Taranto, Italy
Received 2024 January 21; revised 2024 May 20; accepted 2024 May 20; published 2024 June 19

Abstract

The Parker Solar Probe's discovery that magnetic switchbacks and velocity spikes in the young solar wind are abundant has prompted intensive research into their origin(s) and formation mechanism(s) in the solar atmosphere. Recent studies, based on in situ measurements and numerical simulations, argue that velocity spikes are produced through interchange magnetic reconnection. Our work studies the relationship between interplanetary velocity spikes and coronal brightenings induced by changes in the photospheric magnetic field. Our analysis focuses on the characteristic periodicities of velocity spikes detected by the Proton Alpha Sensor on the Solar Orbiter during its fifth perihelion pass. Throughout the time period analyzed here, we estimate their origin along the boundary of a coronal hole. Around the boundary region, we identify periodic variations in coronal brightening activity observed by the Atmospheric Imaging Assembly onboard the Solar Dynamics Observatory. The spectral characteristics of the time series of in situ velocity spikes, remote coronal brightenings, and remote photospheric magnetic flux exhibit correspondence in their periodicities. Therefore, we suggest that the localized small-scale magnetic flux within coronal holes fuels a magnetic reconnection process that can be observed as slight brightness augmentations and outward fluctuations or jets. These dynamic elements may act as mediators, bonding magnetic reconnection with the genesis of velocity spikes and magnetic switchbacks.

Unified Astronomy Thesaurus concepts: Interplanetary magnetic fields (824); Solar wind (1534); Solar coronal transients (312); Supergranulation (1662)

Supporting material: animation

1. Introduction

Solar wind measurements have extensively shown the presence of frequent magnetic field reversals (namely switchbacks), especially in the fast wind at different heliocentric distances (Matteini et al. 2014; Borovsky 2016), although they have been recently found to be ubiquitous also in the slow wind with a strong Alfvénic character (D'Amicis et al. 2021b) in the inner heliosphere. Indeed, recent observations by the Parker Solar Probe (PSP) mission within a heliocentric distance of 0.3 au have mainly observed this solar wind regime and reveal the presence of switchbacks occurring in conjunction with velocity spikes (Bale et al. 2019; Zank et al. 2020; Shi et al. 2022). The radial evolution of velocity and temperature within velocity spikes suggests that their dissipation contributes to the energization of the near-Sun solar wind (Froment et al. 2021; Hou et al. 2023; Suen et al. 2023). The proton temperature anisotropy inside velocity spikes (Luo et al. 2023) can provide favorable conditions for instability and wave mode excitation, including kinetic Alfvén waves (Malaspina et al. 2022) and

ion-acoustic waves (Mozer et al. 2021), which have been observed within and near velocity spikes. Given the likely importance of velocity spikes and magnetic switchbacks for the energetics of the solar wind, determining their origin has become an important research task.

According to in situ measurements, switchbacks occur in bursts or patches with a cross-track spatial scale of $1^{\circ}.1\sim4^{\circ}.4$, consistent with the spatial scale ($1^{\circ}.6\sim6^{\circ}.2$) of solar supergranulation (Fargette et al. 2021). The comparable spatial size of the supergranulation and the size of velocity spikes patches modulated by microstreams points to a potential link between the spikes and magnetic field activity at supergranulation boundaries (Bale et al. 2021; Fargette et al. 2021), such as interchange magnetic reconnection (Drake et al. 2021; He et al. 2021). Further analysis of velocity spike patches reveals an increased α-particle abundance and temporal asymmetry in microstreams, aligning with the expectations associated with interchange magnetic reconnection as a possible source (Bale et al. 2021; Fargette et al. 2021). To distinguish the type of transient activities, Kumar et al. (2023) analyze remote imaging of the Sun at extreme-ultraviolet wave bands and find that the emission intensity at the base of the plume structures presents a similar variation period (10∼20 minutes) as the duration time of velocity spike patches. Gannouni et al. (2023) simulate plume structures triggered by interchange magnetic reconnection and find the release of velocity spikes at a characteristic periodicity of about 20 minutes. During the development of the plumes, small jets (jetlets) and transient brightenings could, therefore, be the result of magnetic reconnection, increasing bulk flow kinetic energy to plumes (Raouafi & Stenborg 2014) and leading to intermittent outflows and thus velocity spikes (Raouafi et al. 2023).

The coronal brightenings accompanied by plumes or smaller plumelets (Kumar et al. 2023) are observed as bright pixels in remote images due to the conversion from jets' kinetic energy to turbulent energy (Ruan et al. 2023) and are observed more easily than jets, especially when the jets are positioned on the solar disk (rather than near the solar limb) and blend with the surrounding coronal radiation, making the jets less distinguishable. Thus, the small brightenings deserve more attention. In this work, we focus on the small brightenings and refer to them as coronal brightenings (CBs). We check the magnetic connectivity between the interplanetary velocity spikes and the CBs in order to draw a robust conclusion on the source region of velocity spikes. We begin with the analysis of in situ measurements of velocity spikes in Section 2 and estimate the source region using magnetic models of the solar atmosphere. Then, we provide an analysis of the remote images in Section 3 and the connection between in situ data and remote sensing in Section 4. We summarize and discuss the results in Section 5.

2. Recurrence of In Situ Velocity Spike Patches

The Proton Alpha Sensor (Owen et al. 2020; Louarn et al. 2021) onboard Solar Orbiter (Solar Orbiter/SWA-PAS; Müller et al. 2020) provides measurements of the proton moments in the solar wind with a time resolution of 4 s. During the time interval of 2022 October 19 to 2022 October 28, at a heliocentric distance of about 0.37 au, the Solar Orbiter Magnetometer (Horbury et al. 2020) measures a series of rapid reversals in the magnetic field radial component called magnetic kinks/switchbacks (Figure 1(a)) correlated with rapid increases in the radial speed of the solar wind, known as velocity spikes (Figure 1(b)). The correlation coefficient CC_{V_n,B_n} is computed using a sliding window at a 30 minutes scale and considering the normal component only in the RTN coordinate frame, which is more Alfvénic than the other two components (Tu et al. 1989; D'Amicis et al. 2021a). Figure 1(c) shows a long and stable Alfvénic interval characterized by correlation coefficients close to -1 from October 19 to 27. This subinterval is also characterized by large amplitude fluctuations in the presence of almost incompressible conditions (almost constant number density and magnetic field magnitude, not shown here) typical of Alfvénic streams as observed in previous studies (e.g., D'Amicis et al. 2021b, and references therein). Both the magnetic switchbacks and velocity spikes tend to occur in bursts or patches (Bale et al. 2021; Fargette et al. 2021).

The speed profile of the radial component exhibits one-sided large amplitude velocity fluctuations (Gosling et al. 2009), which is in agreement with the prediction by Matteini et al. (2014). The velocity variations are of the order of several tens of km s^{-1}, on typical timescales of 6∼10 hr, attributed to the so-called "microstreams" first observed by Ulysses in the fast polar wind (Neugebauer et al. 1997) and in Helios observations close to the Sun (Horbury et al. 2018). These structures have been interpreted as the in situ signature of reconnection jets by Neugebauer (2012), due to newly emerging brightpoint loops with previously open magnetic fields (see, e.g., Subramanian et al. 2010) present in the chromospheric network. Similar large-scale structures are also observed in proton plasma properties in the presence of Alfvénic features (Borovsky 2016).

The wavelet transforms (Fargette et al. 2021) are performed on the time series of the radial velocity (Figure 1(f)) using a Morlet mother wavelet (Torrence & Compo 1998), implemented through the PyCWT Python package.[19] As our work focuses on spike patches, the short-period (∼tens of minutes) component in the wavelet transform spectrum is not displayed. Readers interested in short-period components of velocity spikes may refer to the work of Fargette et al. (2021) and Kumar et al. (2023). In the 2D wavelet power spectrum (Figure 1(g)) and in the global average power spectrum (Figure 1(h)), prominent periodicities are significant from 6 to 10 hr, with a maximum at 7.5 hr. The peak power is significantly stronger than the power of red noise and has a confidence level of 95%. Similar analyses of measurements made during PSP's Encounter 5 show patches of switchbacks lasting from 5 to 18 hr (Fargette et al. 2021), consistent with our results. Considering the strong correlation (Figure 1(c)) between the interplanetary magnetic field and solar wind velocity, we also conduct a wavelet transform analysis on the radial magnetic component in Figure 1(e) and find the data gap in Figure 1(f) does not affect the spectral peak.

3. Recurrence of Coronal Brightenings

According to the two-step ballistic backmapping method[20] (Rouillard et al. 2020), which consists of a potential field source surface (PFSS) model and a Parker spiral model (Altschuler & Newkirk 1969; Schatten et al. 1969), the solar magnetic footpoints of Solar Orbiter during the time interval in Figure 1(f) are concentrated and fall within the field of view of

[19] https://pypi.org/project/pycwt/
[20] http://connect-tool.irap.omp.eu/

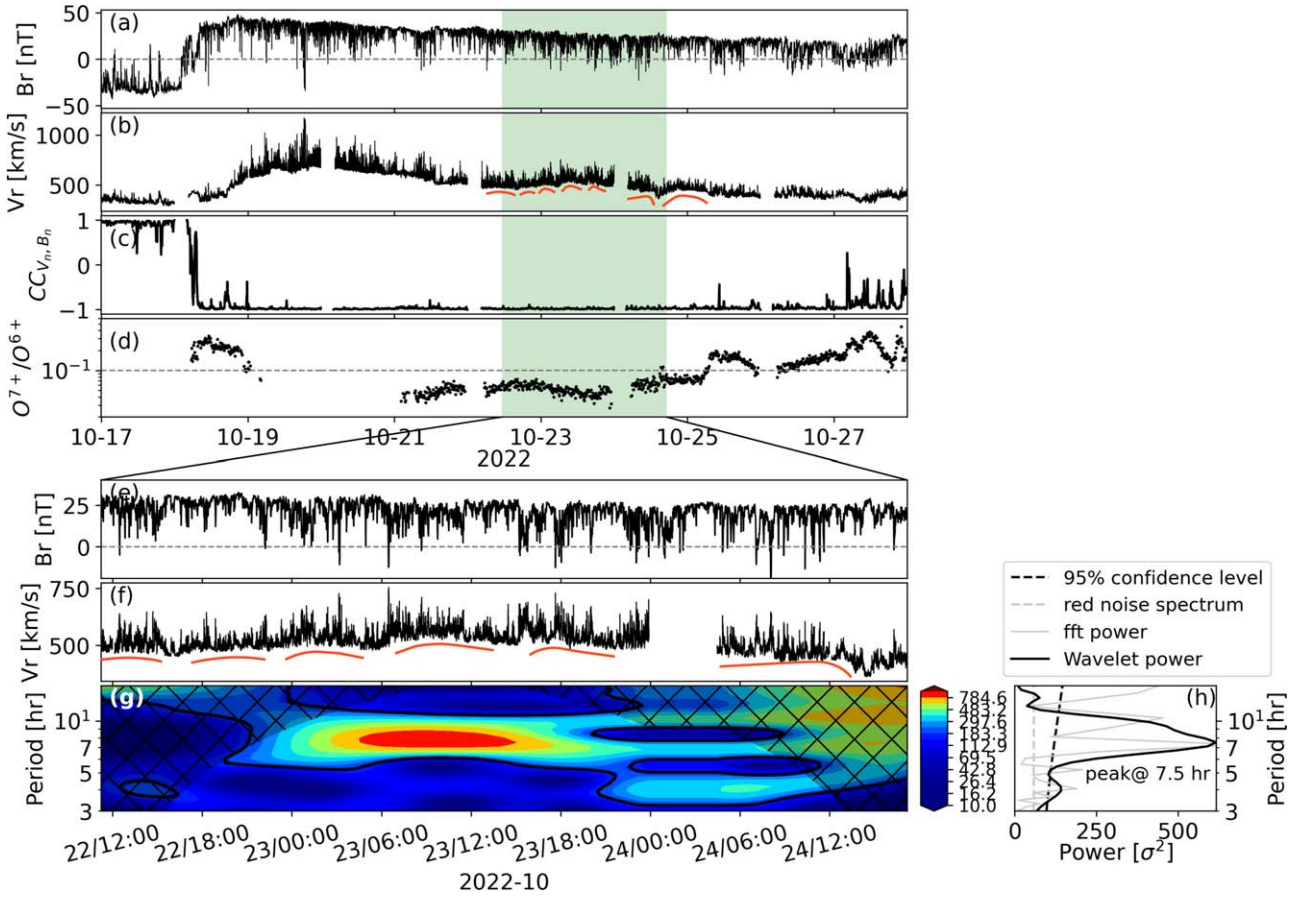

Figure 1. (a) The radial component of the magnetic field measured by Solar Orbiter. (b) The radial solar wind speed measured by Solar Orbiter. The red curves identified visually mark the patches of spikes. The green shaded interval indicates when the solar footpoints of the solar wind are concentrated and remain within the visible disk from Earth. (c) The correlation coefficient between the N component of the magnetic field and the solar wind velocity in the RTN coordinate system. (d) $\frac{O^{7+}}{O^{6+}}$ measured by Solar Orbiter/SWA-HIS. (e) The radial magnetic field during the interval marked with a green shaded area. (f) The radial solar wind speed during the same interval. (g) Wavelet transform power 2D-spectrum of the radial solar wind speed in (f). The black crossed area marks the parameter space outside the confidence level of 95%. (h) The global average of the power spectrum (black solid line) with a peak at a period of 7.5 hr.

the Atmospheric Imaging Assembly (AIA; Lemen et al. 2012) and of the Helioseismic and Magnetic Imager (HMI; Scherrer et al. 2012) onboard Solar Dynamics Observatory (SDO; Pesnell et al. 2012), as shown in Figure 2(a) created by the Propagation Tool[21] (Rouillard et al. 2017). The footpoints concentrate on the boundary of an isolated coronal hole adjacent to an active region (Figure 2(b)). Two kinds of magnetograms (National Solar Observatory GONG and ADAPT GONG) as the boundary conditions of the PFSS model give consistent tracing results, enhancing confidence in the correct identification of the solar source regions of the solar wind.

Due to the typically lower electron temperatures in coronal hole regions compared to quiet-Sun and active regions, the abundance of high ionization components of the heavy ions is lower in coronal holes, such as a lower $\frac{O^{7+}}{O^{6+}}$ compared to the quiet-Sun and active regions. Therefore, in situ measurements of $\frac{O^{7+}}{O^{6+}}$ can be used to verify the reliability of the solar source regions of solar wind given by the backmapping method. The Solar Orbiter/SWA-HIS instrument (Owen et al. 2020) provides the abundance ratio of $\frac{O^{7+}}{O^{6+}}$ (Figure 1(d)) with a time cadence of 10 minutes. Before October 21, the backmapping footpoints move gradually from active regions to the boundary of a coronal hole, corresponding to a transition from high $\frac{O^{7+}}{O^{6+}}$ to low $\frac{O^{7+}}{O^{6+}}$. From October 22 to October 24, the identified source regions of the solar wind remain at the boundary of the coronal hole, and $\frac{O^{7+}}{O^{6+}}$ consistently maintains at a value below 0.1. After October 25, the footpoints gradually move to a smaller and weaker coronal hole, corresponding to a gradual increase of $\frac{O^{7+}}{O^{6+}}$ from below 0.1 to above 0.1. Within the time interval of interest (shaded area in Figure 1), $\frac{O^{7+}}{O^{6+}}$ consistently remains at a low level, suggesting that the solar wind originates from a coronal hole rather than a quiet-Sun region or an active region. This finding is in agreement with the result of our backmapping method. In addition, the $\frac{O^{7+}}{O^{6+}}$ does not show spikes like the velocity spikes. We propose two potential explanations for this behavior: (1) the weak temperature enhancement related to the velocity spikes during this interval, and (2) the cadence of HIS data may not be high enough to pick up temperature variations of less than a few minutes from the small CBs. The detection of these comparatively lower charge state ratios of O-ions (such as $\frac{O^{7+}}{O^{6+}}$) gives us further confidence that the solar wind detected by the Solar Orbiter originates in a coronal hole instead of a quiet-Sun region or an active region.

[21] http://propagationtool.cdpp.eu/

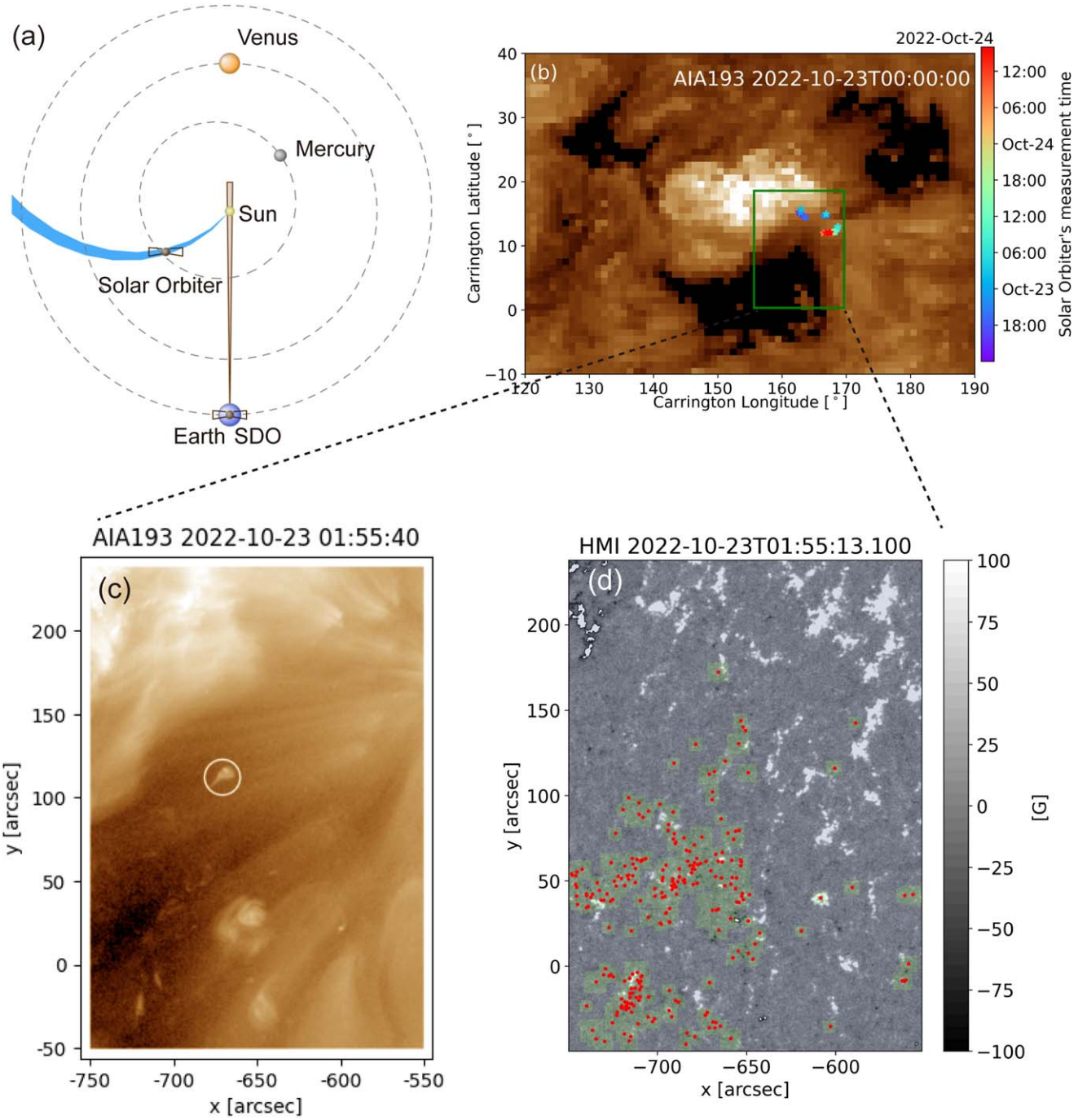

Figure 2. (a) A view of the ecliptic plane with the position of Solar Orbiter and the Parker spiral (blue) connecting Solar Orbiter to the Sun. The brown area shows the field of view of SDO AIA/HMI. (b) The stars represent the footpoints scattered on the synoptic map of AIA 193 Å, and the color of the stars corresponds to the measurement time of the solar wind by Solar Orbiter. (c) An example of identified CB surrounded by a white circle. (d) All CBs' positions (red points) are scattered on the HMI magnetogram. The green boxes around each CB show the diameters of the enclosing circles of each CB and are used to calculate the magnetic flux. An animation of panel (c) is available. The animation shows the positions of all identified CBs on the AIA 193 Å images. The animation contains the AIA 193 Å images during the observation time from 2022 October 21 14:05:40 to 2022 October 24 01:55:40 with a time cadence of 10 minutes. The video lasts 14 s in real time with a framerate of 25 frames s^{-1}.

(An animation of this figure is available.)

Near this coronal hole boundary, many sudden CBs are present in the observations of SDO/AIA. These CBs have a typical lifetime of less than or equal to 10 minutes. We develop a technique to exploit remote-sensing images in 193 Å provided by SDO/AIA to identify CBs automatically in the coronal hole boundary. We calibrate AIA 193 Å images and remove the extreme image pixels by setting color mapping between the 1st and 99.9th percentile of pixel values. We use the OpenCV-python package[22] to detect CBs. Initially, we convert the color format of each AIA 193 Å image into the Hue-Saturation-Value (HSV) format, which has the advantage of distinguishing the brightness and color of image pixels.

[22] https://pypi.org/project/opencv-python/

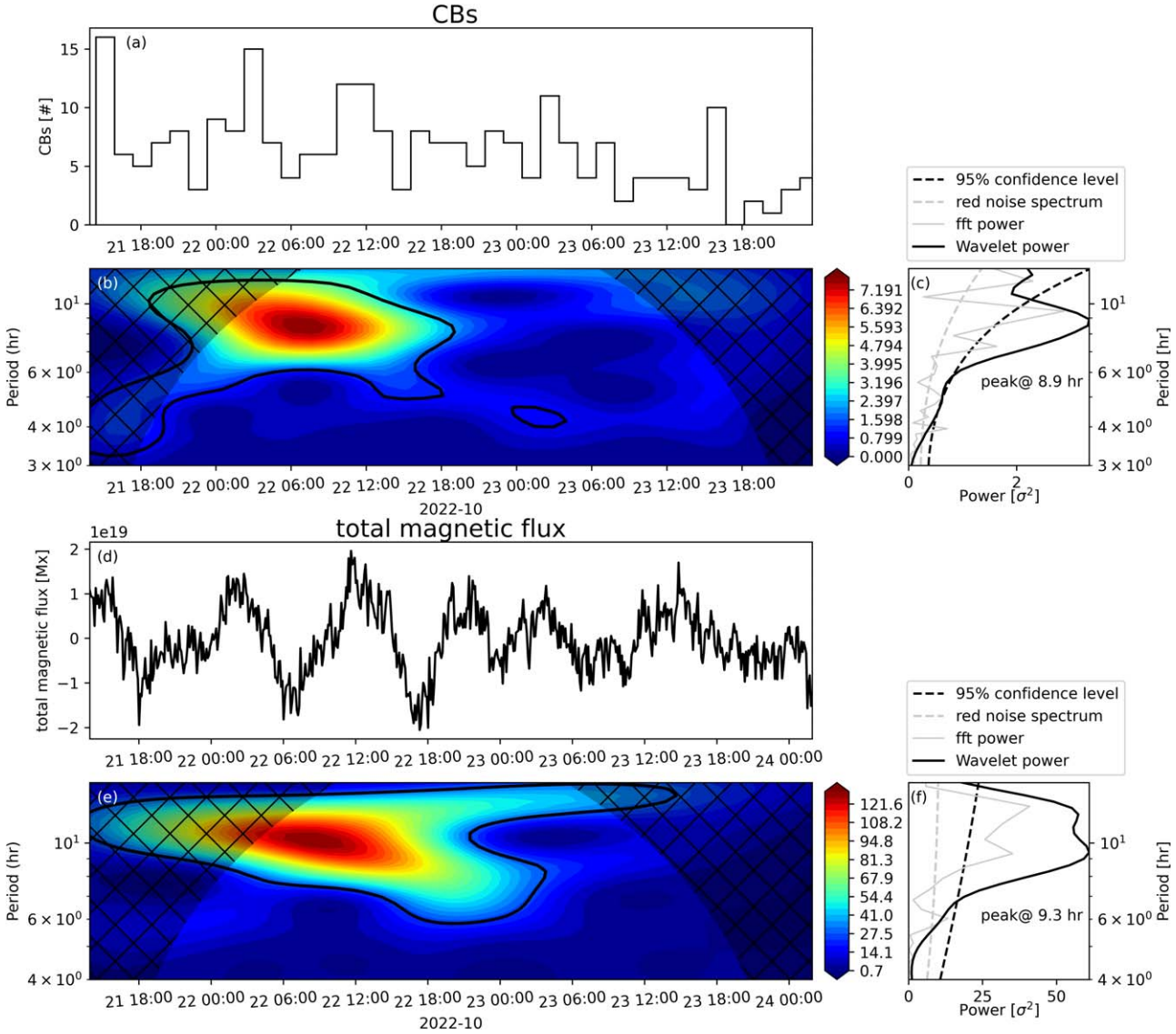

Figure 3. (a) The time series of the number of identified CBs. (b) The wavelet transform power 2D-spectrum of the time series in (a). The black crossed area marks the parameter space outside the confidence level of 95%. (c) The time average power spectrum, fast Fourier transform (fft) power, red noise spectrum, and 95% confidence level. (d)–(f) The same format as (a)–(c) but for the time series of total magnetic flux on the solar surface.

Subsequently, we calculate differential HSV images at a cadence of 10 minutes. To remove the impact of random noise points, dilation with a kernel of 33 rectangular structuring elements is applied to differential images. In each differential image, the contiguous groups of pixels with a differential value of hue within $[-0.03, 0.03]$, differential value of saturation less than -0.1, and differential value of brightness within $[0.1, 1.0]$ are defined as CBs. The CBs covering an area of more than 4000 arcsec^2 are disregarded to eliminate the impact of large bright active regions. Finally, we calculate the minimum enclosing circles of CBs to obtain their position and size. Typically, these CBs last for the duration of one image, which corresponds to 10 minutes. All CBs identified automatically can be found in the animation of Figure 2(c). Through manual inspection of the AIA 193 Å images, we confirm that the specified parameters are suitable for identifying CBs near the current coronal hole boundary. These parameters are not necessarily universally applicable to other solar surface regions, but widely applicable methods, such as empirical mode decomposition techniques developed by De Pablos et al. (2021) and artificial neural networks, may resolve this shortcoming. However, our automatic analysis of AIA images allows us to map the occurrence of CBs.

In Figure 2(d), the red points mark the centers of the CBs, and the side lengths of the green squares around each CB are comparable to the diameters of the enclosing circles. The entire green area in the SDO/HMI magnetogram is used to obtain the time series of unsigned magnetic flux only beneath the CBs, mitigating the influence of the magnetic field from active regions. In Figure 3(a), the duration of each bin is 90 minutes, a value chosen to be both less than the minimum period we are interested in and long enough to contain more CBs in each bin. For the time series of unsigned magnetic flux (Figure 3(d)), the signals over 15 hr are filtered out using a low-pass filter to remove long-period variations. Based on visual inspection, some correlations appear between the two time series in Figures 3(a) and (d), especially for the first half of both time series. The prominent signals in the wavelet 2D-spectrum for the time series of the number of CBs and unsigned magnetic flux (Figures 3(b) and (e)) are located at similar times and

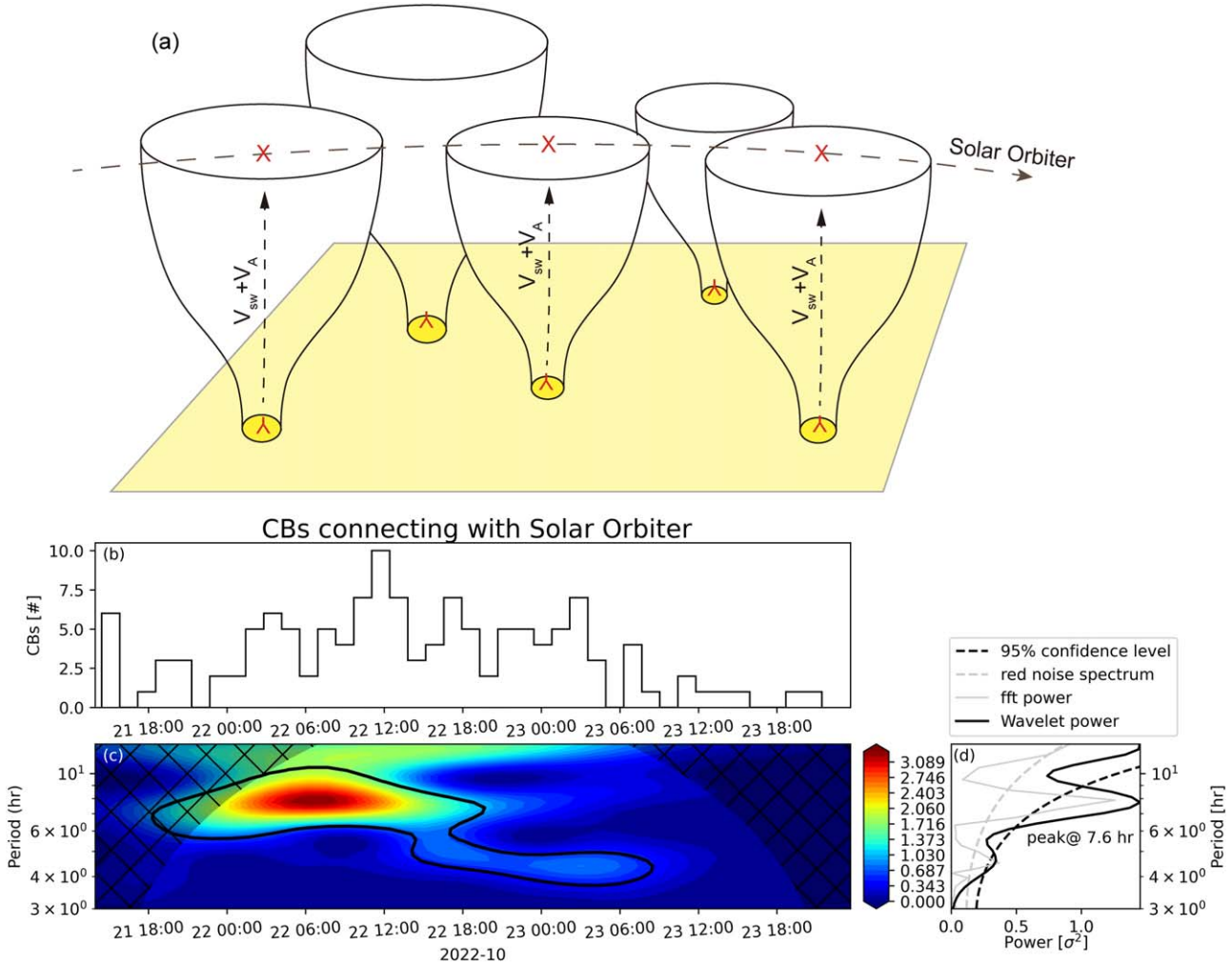

Figure 4. (a) Animation of the proposed scenario that connects CBs with the in situ measurements by Solar Orbiter. (b)–(d) The same format as Figures 3(a)–(c) but for the time series of the number of CBs connecting with Solar Orbiter.

periods. For the CBs, the periodical signal is significant within the period from 6 to 10 hr and peaks at a period of 8.9 hr (Figures 3(b) and (c)). Regarding the unsigned magnetic flux, the peak period is approximately 9.3 hr (Figures 3(e) and (f)). The periodicity and correlation are weak for the second half of both time series. However, the reason for the presence and weakening of the periodicity of magnetic flux remains elusive.

To capture the fine signals of CBs, we create AIA 193 Å imaging animations of all CBs (249 in total) with a time duration of 10 minutes and a time resolution of 12 s. We classify the CBs into three categories: (1) CBs clearly showing loop- or anemone-shaped bases (122 events), (2) CBs only showing a brightening (119 events), and (3) only showing material flow (8 events). Among the 122 CBs with clear loop or anemone-shaped bases, 88 CBs exhibit distinct jet signals, accounting for over 70%. The total number of CBs showing jet signals is 96 (=88 + 8), accounting for approximately 38%, more than one-third of the total.

4. Connecting Interplanetary Velocity Spikes and Solar Coronal Brightenings

We develop a new technique to exploit our CB mapping and connect the CBs to the solar wind interval measured by Solar Orbiter. First, based on thermodynamic MHD coronal simulations provided by Predictive Science Inc. (PSI),[23] we trace the magnetic field lines rooted at our identified CBs and therefore obtain their coordinates and cross sections. By considering the orbit of Solar Orbiter, we determine whether the spacecraft passes magnetic flux tubes that are connected to the CBs. Second, since velocity spikes are Alfvénic perturbations and the propagation speed of the switchbacks in the solar wind flow reference frame is approximately the local Alfvén speed (Shoda et al. 2021), we assume that transient fluctuations released from each CB propagate outward along the magnetic flux tube at a propagation speed equal to the Alfvén speed (V_A) plus the solar wind speed (V_{sw}). The Alfvén speed and solar wind velocity are obtained from the thermodynamic MHD model.

Combining the occurrence time of CBs, the switchback propagation time, and the Solar Orbiter ephemeris, we estimate when Solar Orbiter should detect the fluctuations launched from each CB. During this process, we remove any CBs that are not associated with Solar Orbiter. Hence, we convert the time series of the number of CBs at the surface shown in Figure 3 to a calibrated time series of the number of CBs that we expect to cause a velocity spike measured by Solar Orbiter. The calibrated time series of CBs is shown in Figure 4(b). We

[23] https://www.predsci.com/mhdweb/data_access.php

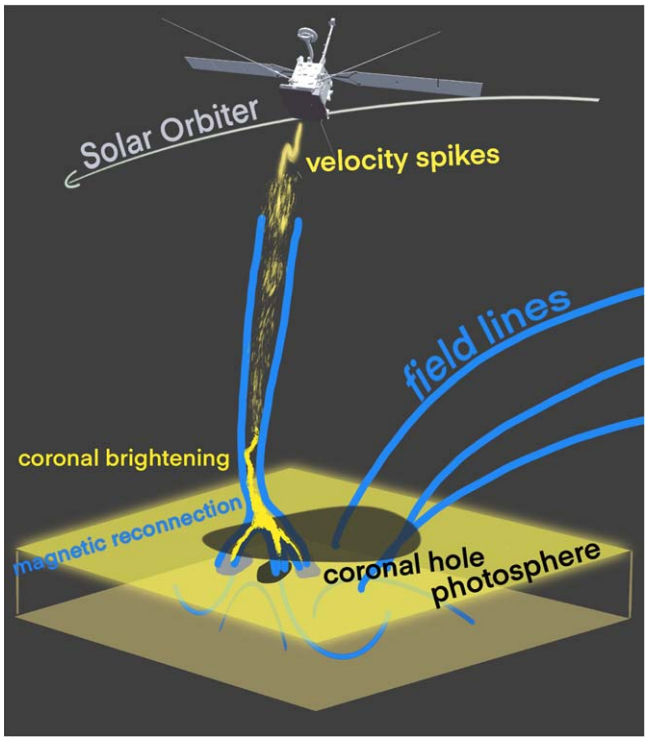

Figure 5. Our scenario about the formation of velocity spikes. The closed magnetic loop caused by flux emergence, cancellation, or shearing motions reconnects with surrounding open field lines. During the reconnection processes, the accumulated magnetic energy is released to heat the surrounding plasma, and the increasing brightness becomes visible as a CB. Waves and jets are triggered as seeds of the switchbacks and velocity spikes measured by Solar Orbiter.

perform a wavelet transform on the calibrated time series and obtain the relevant power spectrum in Figures 4(c) and (d). The obtained peak power occurs at a period of about 7.6 hr, which is less than the 8.9 hr given in the original CB time series (Figure 3) and more consistent with the peak period (7.5 hr) of the in situ velocity spikes (Figures 1(f) and (g)). After considering the broadening of the flux tubes and the geometry of Solar Orbiter trajectories across them, the removal of irrelevant CBs from the original time series reduces the periodicity from 8.9 hr to 7.6 hr. In addition, the time lag between the two signal peaks in the 2D-spectrum (Figure 1(g) and Figure 4(c)) is consistent with the propagation time from the solar surface to the orbit of Solar Orbiter. The propagation time is estimated as 25 hr based on the spikes' velocity ($600\,\mathrm{km\,s^{-1}}$) measured by Solar Orbiter at 0.37 au or as 23 hr from the radial profile of $V_A + V_{sw}$ provided by the MHD model.

5. Summary and Discussion

Among our observed CBs with clearly defined base structures, the proportion exhibiting jet characteristics exceeds 70%. Considering factors such as the lack of detectability of jets that are parallel to the observation direction and inconspicuous X-ray jets (Sterling et al. 2022), it is highly likely that some jets are missed. Therefore, 70% represents a lower limit of this proportion. We speculate that the reason for the missing observation of bases or material flows in 119 CBs lies in the insufficient spatial resolution of our observations. These CBs are potentially associated with jets smaller than the AIA 193 Å imaging resolution, as reported by Tian et al. (2014), or similar to the campfires (Chen et al. 2021), which are usually accompanied by small-scale jets (Panesar et al. 2021). Although we do not have Solar Orbiter/EUI-HRI observations of the coronal hole boundaries, we speculate that the proportion of these CBs corresponding to jets also likely exceeds 70%. Some of these jets are potentially oriented along open magnetic field lines ejecting materials into the nascent solar wind, while others are oriented along closed magnetic loops transporting material within the reconfigured closed loops.

Magnetic reconnection is a probable process for generating jets and CBs (Shibata et al. 1992). Supportive evidence is the positive correlation and similar periodicity of the time series of CBs and magnetic flux shown in Figure 3, consistent with previous studies (Innes & Teriaca 2013; Young & Muglach 2014; Panesar et al. 2016; Kumar et al. 2019; Muglach 2021). The magnetic field environment of the coronal hole is also suitable for magnetic reconnection between open field lines and closed magnetic loops. In other studies, Young & Muglach (2014) find magnetic field cancellation at locations of CBs with mixed polarity. This kind of magnetic flux cancellation is generally considered a triggering mechanism for quiet-Sun coronal jets (Innes & Teriaca 2013; Panesar et al. 2016).

We provide a scenario, shown in Figure 5, to explain the formation of jets, CBs, and velocity spikes. The accumulated magnetic energy is released by reconnection between closed loops and surrounding open field lines. The trigger of magnetic reconnection remains to be discussed, and magnetic cancellation associated with bipolar magnetic convergence is likely to trigger reconnection (Panesar et al. 2016; Muglach 2021). For example, Panesar et al. (2016) suggest that magnetic cancellation results in highly sheared mini-filament fields beyond critical values, thereby triggering internal reconnection and subsequent eruption of the mini-filaments. Other processes, such as flow shear and magnetic emergence, may also lead to reconnection eruptions. For example, most events studied by Kumar et al. (2019) do not show a noticeable flux emergence or cancellation associated with jet eruptions. They suggest that shearing or rotational photospheric motions provide the energy stored in the mini-filaments for the subsequent eruption.

During the reconnection process, the released magnetic energy heats the surrounding plasma, and the increasing brightness is visible as a CB. In addition to thermal energy (Shen et al. 2018), waves and jets released during the reconnection processes propagate outward and form velocity spikes in the solar wind (Sterling et al. 2020; Neugebauer & Sterling 2021; Moore et al. 2023). The detailed process of how jets and waves evolve into velocity spikes is not clear, but there are some proposed explanations. The reversing of magnetic field lines due to the shear-driven Kelvin–Helmholtz instability triggered by the propagation of jets (Wei et al. 2023) is a potential source of switchbacks. In addition, the super-Parker spiral resulting from fast-speed jets overtaking the background solar wind (Schwadron & McComas 2021) may also cause the reversing of magnetic field lines. The evolution of waves generated by magnetic reconnection may also play an important role in generating switchbacks (Sterling & Moore 2020; He et al. 2021; Mallet et al. 2021; Hou et al. 2023). To a varying degree but ultimately in all of these scenarios, CBs can serve as a way to count switchbacks, reveal their origin, and further quantify the influence of magnetic

activity, such as magnetic reconnection, on the state of the corona and solar wind. It thus improves the accuracy of coronal and heliospheric simulations.

Regarding the generation of jets, CBs, and switchbacks, Sterling et al. (2015) propose an eruptive reconnection model based on observational analysis, where CBs arise from internal reconnection associated with microflare bursts. In this scenario, jets originate from interchange reconnection between magnetic flux ropes and external open fields. This not only explains the correlation between CBs and jets but also accounts for the associated magnetic activity. Our schematic diagram resembles the eruptive models of jets and switchbacks by Sterling et al. (2015) and Sterling & Moore (2020). However, our work takes this idea further by using observational data and magnetic connectivity to establish a connection between solar magnetic reconnection shown in Figure 5 and in situ velocity spikes.

Acknowledgments

We acknowledge the solar wind measurements from Proton Alpha Sensor (PAS) onboard Solar Orbiter, remote sensing imagery SDO, magnetograms from GONG, and coronal simulations provided by Predictive Science Inc. Solar Orbiter is a space mission of international collaboration between ESA and NASA, operated by ESA. Solar Orbiter Solar Wind Analyser (SWA) data are derived from scientific sensors that have been designed and created, and are operated under funding provided in numerous contracts from the UK Space Agency (UKSA), the UK Science and Technology Facilities Council (STFC), the Agenzia Spaziale Italiana (ASI), the Centre National d'Etudes Spatiales (CNES, France), the Centre National de la Recherche Scientifique (CNRS, France), the Czech contribution to the ESA PRODEX program and NASA. The work at Peking University is supported by NSFC, NKRDPC, and CNSA (42241118, 42174194, 2021YFA0718600, 2022YFF0503800, 42150105, 42204166, D050106, D050103). The work at IRAP is funded by the ERC SLOW_SOURCE project (SLOW_SOURCE-DLV-819189). C.-P.H. is also supported by the China Scholarship Council (202206010136). Solar Orbiter SWA work at UCL/MSSL was funded under STFC grants ST/T001356/1, ST/S000240/1, and ST/X002152/1. C.J.O. and D.V. are supported by STFC Consolidated Grant ST/W001004/1. N. F. was supported by STFC grant ST/W001071/1. This research was supported by the International Space Science Institute (ISSI) in Bern through ISSI International Team project #463 (Exploring The Solar Wind In Regions Closer Than Ever Observed Before) led by L. Harra. We also acknowledge helpful discussions within the ISSI team 'Unravelling Solar Wind Microphysics in the Inner Heliosphere' led by D. Perrone and S. Toledo-Redondo.

ORCID iDs

Chuanpeng Hou https://orcid.org/0000-0001-7205-2449
Alexis P. Rouillard https://orcid.org/0000-0003-4039-5767
Jiansen He https://orcid.org/0000-0001-8179-417X
Bahaeddine Gannouni https://orcid.org/0000-0002-1711-1802
Victor Réville https://orcid.org/0000-0002-2916-3837
Andrey Fedorov https://orcid.org/0000-0002-9975-0148
Lubomír Přech https://orcid.org/0000-0003-0867-0458
Christopher J. Owen https://orcid.org/0000-0002-5982-4667
Daniel Verscharen https://orcid.org/0000-0002-0497-1096
Raffaella D'Amicis https://orcid.org/0000-0003-2647-117X
Luca Sorriso-Valvo https://orcid.org/0000-0002-5981-7758
Naïs Fargette https://orcid.org/0000-0001-6308-1715
Jesse Coburn https://orcid.org/0000-0002-2576-0992
Vincent Génot https://orcid.org/0000-0002-7708-8077
Jim M. Raines https://orcid.org/0000-0001-5956-9523
Roberto Bruno https://orcid.org/0000-0002-2152-0115
Benoit Lavraud https://orcid.org/0000-0001-6807-8494
Nicolas André https://orcid.org/0000-0001-8017-5676
Rungployphan Kieokaew https://orcid.org/0000-0003-0937-2655
Illya Plotnikov https://orcid.org/0000-0002-0074-4048
Dhiren Kataria https://orcid.org/0000-0002-1034-3854
Frederic Allegrini https://orcid.org/0000-0003-0696-4380
Timothy Horbury https://orcid.org/0000-0002-7572-4690

References

Altschuler, M. D., & Newkirk, G. 1969, SoPh, 9, 131
Bale, S., Badman, S., Bonnell, J., et al. 2019, Natur, 576, 237
Bale, S. D., Horbury, T., Velli, M., et al. 2021, ApJ, 923, 174
Borovsky, J. E. 2016, JGRA, 121, 5055
Chen, Y., Przybylski, D., Peter, H., et al. 2021, A&A, 656, L7
D'Amicis, R., Bruno, R., Panasenco, O., et al. 2021a, A&A, 656, A21
D'Amicis, R., Perrone, D., Bruno, R., & Velli, M. 2021b, JGRA, 126, e28996
De Pablos, D., Long, D. M., Owen, C. J., et al. 2021, SoPh, 296, 68
Drake, J., Agapitov, O., Swisdak, M., et al. 2021, A&A, 650, A2
Fargette, N., Lavraud, B., Rouillard, A. P., et al. 2021, ApJ, 919, 96
Froment, C., Krasnoselskikh, V., de Wit, T. D., et al. 2021, A&A, 650, A5
Gannouni, B., Réville, V., & Rouillard, A. 2023, ApJ, 958, 110
Gosling, J. T., McComas, D. J., Roberts, D. A., & Skoug, R. M. 2009, ApJL, 695, L213
He, J., Zhu, X., Yang, L., et al. 2021, ApJL, 913, L14
Horbury, T., O'brien, H., Blazquez, I. C., et al. 2020, A&A, 642, A9
Horbury, T. S., Matteini, L., & Stansby, D. 2018, MNRAS, 478, 1980
Hou, C., Zhu, X., Zhuo, R., et al. 2023, ApJ, 950, 157
Innes, D. E., & Teriaca, L. 2013, SoPh, 282, 453
Kumar, P., Karpen, J. T., Antiochos, S. K., et al. 2019, ApJ, 873, 93
Kumar, P., Karpen, J. T., Uritsky, V. M., et al. 2023, ApJL, 951, L15
Lemen, J. R., Title, A. M., Akin, D. J., et al. 2012, SoPh, 275, 17
Louarn, P., Fedorov, A., Prech, L., et al. 2021, A&A, 656, A36
Luo, Q., Duan, D., He, J., et al. 2023, ApJL, 952, L40
Malaspina, D. M., Chasapis, A., Tatum, P., et al. 2022, ApJ, 936, 128
Mallet, A., Squire, J., Chandran, B. D., Bowen, T., & Bale, S. D. 2021, ApJ, 918, 62
Matteini, L., Horbury, T. S., Neugebauer, M., & Goldstein, B. E. 2014, GeoRL, 41, 259
Moore, R. L., Tiwari, S. K., Panesar, N. K., & Sterling, A. C. 2023, ApJL, 945, L16
Mozer, F., Bonnell, J., Hanson, E., Gasque, L., & Vasko, I. 2021, ApJ, 911, 89
Muglach, K. 2021, ApJ, 909, 133
Müller, D., Cyr, O. S., Zouganelis, I., et al. 2020, A&A, 642, A1
Neugebauer, M. 2012, ApJ, 750, 50
Neugebauer, M., Ruzmaikin, A., & McComas, D. J. 1997, in AIP Conf. Ser. 385, Robotic Exploration Close to the Sun: Scientific Basis, ed. S. R. Habbal (Melville, NY: AIP), 41
Neugebauer, M., & Sterling, A. C. 2021, ApJL, 920, L31
Owen, C., Bruno, R., Livi, S., et al. 2020, A&A, 642, A16
Panesar, N. K., Sterling, A. C., Moore, R. L., & Chakrapani, P. 2016, ApJL, 832, L7
Panesar, N. K., Tiwari, S. K., Berghmans, D., et al. 2021, ApJL, 921, L20
Pesnell, W. D., Thompson, B. J., & Chamberlin, P. 2012, SoPh, 275, 3
Raouafi, N.-E., & Stenborg, G. 2014, ApJ, 787, 118
Raouafi, N. E., Stenborg, G., Seaton, D. B., et al. 2023, ApJ, 945, 28
Rouillard, A., Lavraud, B., Génot, V., et al. 2017, P&SS, 147, 61
Rouillard, A. P., Pinto, R., Vourlidas, A., et al. 2020, A&A, 642, A2
Ruan, W., Yan, L., & Keppens, R. 2023, ApJ, 947, 67
Schatten, K. H., Wilcox, J. M., & Ness, N. F. 1969, SoPh, 6, 442
Scherrer, P. H., Schou, J., Bush, R., et al. 2012, SoPh, 275, 207
Shen, Y., Liu, Y., Liu, Y. D., et al. 2018, ApJ, 861, 105

Shi, C., Panasenco, O., Velli, M., et al. 2022, ApJ, 934, 152
Shibata, K., Ishido, Y., Acton, L. W., et al. 1992, PASJ, 44, L173
Shoda, M., Chandran, B. D., & Cranmer, S. R. 2021, ApJ, 915, 52
Sterling, A. C., & Moore, R. L. 2020, ApJL, 896, L18
Sterling, A. C., Moore, R. L., Falconer, D. A., & Adams, M. 2015, Natur, 523, 437
Sterling, A. C., Moore, R. L., Panesar, N. K., & Samanta, T. 2020, JPhCS, 1620, 012020
Sterling, A. C., Schwanitz, C., Harra, L. K., et al. 2022, ApJ, 940, 85
Subramanian, S., Madjarska, M. S., & Doyle, J. G. 2010, A&A, 516, A50
Suen, G. H. H., Owen, C. J., Verscharen, D., et al. 2023, A&A, 675, A128
Tian, H., DeLuca, E., Cranmer, S., et al. 2014, Sci, 346, 1255711
Torrence, C., & Compo, G. P. 1998, BAMS, 79, 61
Tu, C. Y., Marsch, E., & Thieme, K. M. 1989, JGR, 94, 11739
Wei, H., Huang, Z., Long, D. M., et al. 2023, A&A, 678, L7
Young, P., & Muglach, K. 2014, SoPh, 289, 3313
Zank, G., Nakanotani, M., Zhao, L.-L., Adhikari, L., & Kasper, J. 2020, ApJ, 903, 1